ENHANCING POOL BOILING HEAT TRANSFER OF MODIFIED SURFACE BY 3-D LATTICE BOLTZMANN METHOD

by

Qiang HUANG [a,b,c], ***Jingzhi ZHOU*** [a,c*], ***Xiulan HUAI*** [a,b,c], ***and Feng ZHOU*** [a,b,c]

[a] Institute of Engineering Thermophysics, Chinese Academy of Sciences, Beijing, China
[b] School of Engineering Science, University of Chinese Academy of Science, Beijing, China
[c] Nanjing Institute of Future Energy System, Nanjing, China

Original scientific paper
https://doi.org/10.2298/TSCI230114121H

In this study, pool boiling from micro-pillar modified surface has been simulated numerically by a 3-D lattice Boltzmann method. Effects of geometries and wettability of micro-pillar on boiling heat transfer performance were also systematically evaluated. Result showed that compared within micro-pillar surface, heat flux of cubic micro-pillar surface was the highest with the lowest wall temperature. In addition, compared to hydrophilic condition, Heat flux of cubic micro-pillar surface with hydrophobic wettability increased by 98.3%. This is because hydrophobic wettability influenced nucleation site density, vapor-liquid-flow field and heat transfer performance much more than cubic shaped geometry. Finally, heat flux of cubic micro-pillar surface with hybrid wettability increased by 430.7% compared to pure hydrophilic wettability. That is due to optimal hybrid wettability surface could control nucleate site location, restrict bubble growth, and increase obviously heat transfer performance.

Key words: *3-D lattice Boltzmann method, pool boiling, micro-pillar, geometry, wettability*

Introduction

Pool boiling is widely used in electronic chip due to its high heat transfer performance [1, 2]. Micro-structure surface [3, 4] plays a key role on enhancing pool boiling heat transfer performances. The nucleation sites due to micro-pillar mainly effect on three important aspects, namely, the onset of the nucleation boiling, the merger of bubbles, and the hydrodynamic action between the vapor phase and liquid phase. Recently, some experiments have been made to enhance nucleate boiling, mainly focusing on modified surfaces including micro/nanostructure and wettability. Ye *et al*. [5] studied the effect of elastic pillar arrays of different pillar spacing on improving critical heat flux (CHF). Xin *et al*. [6] investigated the pool boiling heat transfer performance of bi-structured surface. Shen *et a*l. [7] reported that wettability surfaces significantly increased CHF of the biophilic surfaces due to facilitating bubble nucleation and agitation effect. Koukoravas *et al*. [8] offered those quantitative arguments for incorporating wettability patterning in vapor-chamber technology. Jo *et al*. [9] studied single bubble dynamics of distilled water on hydrophobic/hydrophilic mixed surfaces. Kousalya *et al*. [10] revealed that mixed wettability surface could increase nucleate density and promote bubble nucleation. Xie *et al*. [11] pointed out that gradient wettability surface decreased remarkably thermal resistance

* Corresponding author, e-mail: zhoujingzhi@iet.cn

of the heat pipe. Bourdon *et al*. [12] investigated the influence of wettability on the inception of boiling. Hu *et al*. [13] demonstrated that the wettability gradient enhanced heat transfer coefficient. Besides, latice Boltzmann method (LBM) [14] has been utilized to study boiling nature of artificial nucleation site surfaces. Zhou *et al*. [15] investigated periodic bubble cycle by 3-D LBM. Li *et al.* [16] researched on an innovative modified surface to enhance heat transfer performance by 3-D LBM. Mu *et al*. [17] studied an entire bubble cycle on roughened surfaces. Jiang *et al*. [18] simulated heat transfer happened on micro-channel by neural network.

Through the aforementioned literature review, it seems that relatively few 3-D numerical simulations aiming to the effect of wettability distribution over micro-pillar with different geometries on pool boiling, especially mixed wettability. In this work, 3-D LBM was used to research on the heat transfer performance of micro-pillar structured surface. First, the effect of geometry of micro-pillar surface under hydrophilic circumstance on heat transfer was investigated. Second, the influence of hydrophobic wettability of micro pillar structured surface on pool boiling process was examined. Lastly, the heat transfer process of the hybrid wettability surface was also presented.

Method and model

The 3-D modified pseudo-potential LBM for multi-phase flow

All of equations can be found in [19]. The convolution equation of the particle distribution function is denoted:

$$f_\mathrm{i}(\vec{x}+\vec{e}_\mathrm{i}\delta t, t+\delta t)-f_\mathrm{i}(\vec{x}, t)=-\frac{1}{\tau}\left(f_\mathrm{i}(\vec{x}, t)-f_\mathrm{i}^\mathrm{eq}(\vec{x}, t)\right)+\Delta f_\mathrm{i}(\vec{x}, t) \tag{1}$$

where $f_\mathrm{i}^\mathrm{eq}(\vec{x}, t)$ is the corresponding equilibrium function, which is given:

$$f_\mathrm{i}^\mathrm{eq}=\omega_\mathrm{i}\rho\left[1+\frac{\vec{e}_\mathrm{i}\vec{u}}{c_\mathrm{s}^2}+\frac{(\vec{e}_\mathrm{i}\vec{u})^2}{2c_\mathrm{s}^4}-\frac{\vec{u}^2}{2c_\mathrm{s}^2}\right] \tag{2}$$

where $\omega_0 = 1/3$, $\omega_{1\text{-}6} = 1/18$, $\omega_{7\text{-}18} = 1/36$. The discrete lattice velocity vector $\vec{e}_\mathrm{i}$ are given:

$$e_\mathrm{i}=\begin{cases}(0, 0, 0), & i=0\\ (\pm1, 0, 0)c, (0, \pm1, 0)c, (0, 0, \pm1)c, & i=1\text{-}6\\ (\pm1, \pm1, 0)c, (\pm1, 0, \pm1)c, (0\pm1, \pm1)c, & i=7\text{-}18\end{cases} \tag{3}$$

The ν is calculated by:

$$\nu=c_\mathrm{s}^2(\tau_\mathrm{a}-0.5)\delta t \tag{4}$$

The ν at the liquid-vapor interface, is given:

$$\nu=\nu_\ell\frac{\rho-\rho_\mathrm{v}}{\rho_\ell-\rho_\mathrm{v}}+\nu_\mathrm{v}\frac{\rho_\ell-\rho}{\rho_\ell-\rho_\mathrm{v}} \tag{5}$$

The exact difference method implements force into the LBM resulting in better accuracy. The force source term is written:

$$\Delta f_\mathrm{i}(\vec{x}, t)=f_\mathrm{i}^\mathrm{eq}(\rho(\vec{x}, t), \vec{u}+\Delta\vec{u})-f_\mathrm{i}^\mathrm{eq}(\rho(\vec{x}, t), \vec{u}) \tag{6}$$

where $\Delta\vec{u} = \vec{F}\delta t/\rho$ is the change of velocity caused by force $\vec{F}$ during time step δt. The $\vec{F}$ is given:

$$\vec{F}=\vec{F}_\mathrm{coh}+\vec{F}_\mathrm{ads}+\vec{F}_\mathrm{grav} \tag{7}$$

The inter-particle interaction force $\vec{F}_{\text{coh}}$ is given:

$$\vec{F}_{\text{coh}} = -\beta\psi(\vec{x})\sum_i G(\vec{x}+\vec{e}_{\text{i}}\delta t)\psi(\vec{x}+\vec{e}_{\text{i}}\delta t)\vec{e}_{\text{i}} - \frac{1-\beta}{2}\sum_i G(\vec{x}+\vec{e}_{\text{i}}\delta t)\psi^2(\vec{x}+\vec{e}_{\text{i}}\delta t)\vec{e}_{\text{i}} \tag{8}$$

where β is the given by particular equation of state and G – the interaction strength which is written:

$$G(\vec{x}+\vec{e}_{\text{i}}\delta t) = \begin{cases} \text{g}, & |\vec{e}_{\text{i}}| = 1 \\ \dfrac{\text{g}}{2}, & |\vec{e}_{\text{i}}| = \sqrt{2} \\ 0, \text{ otherwise} \end{cases} \tag{9}$$

The $\psi(\vec{x})$ is given:

$$\psi(\vec{x}) = \sqrt{\frac{2(p-\rho c_{\text{s}}^2)}{c_0 \text{g}}} \tag{10}$$

where c_0 is equates to 6 in D3Q19. The P-R EOS is adopted in this simulation, which is given:

$$p = \frac{\rho \text{R} T}{(1-b\rho)} - \frac{a\rho^2 \Phi_0(T)}{1+2b\rho-b^2\rho^2}$$
$$\Phi_0(T) = \left[1+\left(0.37464+1.54226w-0.26992w^2\right)\left(1-\sqrt{\frac{T}{T_{\text{cr}}}}\right)\right]^2 \tag{11}$$

where $w = 0.344$, $a = 2/49$, $b = 2/21$, R = 1. and $T_{\text{cr}} = 0.0729$.

The fluid-solid interaction force $\vec{F}_{\text{ads}}$ is given:

$$\vec{F}_{\text{ads}} = -G_{\text{ads}}\psi(\vec{x})\sum_i \omega_{\text{i}} s(\vec{x}+\vec{e}_{\text{i}}\delta t)\,\vec{e}_{\text{i}} \tag{12}$$

where G_{ads} is the fluid-solid interaction strength, which is implemented to control contact angle of surface, $s(\vec{x}+\vec{e}_{\text{i}}\delta t)$is an indicator function with $s = 1$ for solid and $s = 0$ for fluid.

The gravitational force is given:

$$\vec{F}_{\text{grav}} = (\rho(\vec{x}) - \rho_{\text{aver}})\vec{\text{g}}_{\text{grav}} \tag{13}$$

where $\vec{\text{g}}$ is the gravitational acceleration.

The macroscopic density ρ and velocity $\vec{u}$ of fluid are defined:

$$\rho = \sum_i f_{\text{i}} \tag{14}$$

$$\rho\vec{u} = \sum_i f_{\text{i}}\vec{e}_{\text{i}} \tag{15}$$

The real fluid velocity $\vec{U}$ is described:

$$\vec{U} = \vec{u} + \frac{\delta t}{2\rho}\vec{F} \tag{16}$$

Energy equation models

The evolution equation for temperature distribution function:

$$g_{\text{i}}(\vec{x}+\vec{e}_{\text{i}}\delta t, t+\delta t) - g_{\text{i}}(\vec{x}, t) = -\frac{1}{\tau_T}\left(g_{\text{i}}(\vec{x}, t) - g_{\text{i}}^{\text{eq}}(\vec{x}, t)\right) + \delta t\omega_{\text{i}}\Phi \tag{17}$$

where $g_i^{eq}(\vec{x}, t)$ is the orresponding equilibrium function, which is given:

$$g_i^{eq} = \omega_i T\left[1 + \frac{\vec{e}_i\vec{U}}{c_s^2} + \frac{\left(\vec{e}_i\vec{U}\right)^2}{2c_s^4} - \frac{\vec{U}^2}{2c_s^2}\right] \tag{18}$$

The source term in eq. (17), which is responsible for liquid-vapor phase change, is given:

$$\Phi = T\left[1 - \frac{1}{\rho c_v}\left(\frac{\partial p}{\partial T}\right)_\rho\right]\nabla\vec{U} + \left[\frac{1}{\rho c_v}\nabla(\lambda\nabla T) - \nabla\left(\frac{\lambda}{\rho c_v}\nabla T\right)\right] \tag{19}$$

The temperature is obtained:

$$T = \sum_i g_i \tag{20}$$

The D^2 law [15]

Figure 1(a) shows liquid with low $T = 0.9T_{cr}$ suspended in the central of computation model filled by vapor with high T, when fig. 1(b) depicts the results of radius of fluid temporary change with time under different T_{cr}. At any case in fig. 1(b), the $(D/D_0)^2$ is linear to time, and decrease velocity of it increases with T_v, which is according to D^2 law.

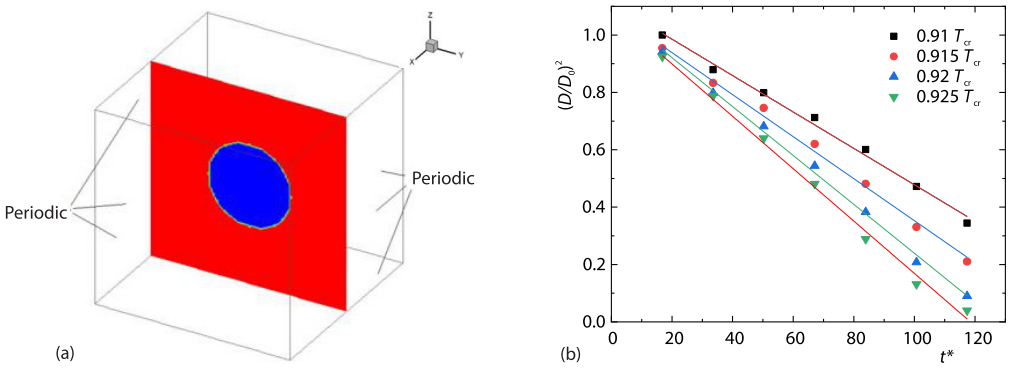

Figure 1. The D^2 law model examination; (a) computation model and (b) radius variation under different T_{cr}

Computation set-up and boundary conditions

Figure 2(a) shows the computation domain with boundary condition. The constant temperature, T_d, is imposed on bottom of the computation domain. The top boundary of simulation domain is constant pressure and temperature boundary conditions, respectively. Conjugate heat transfer and bounce back boundary condition are imposed at solid-liquid interface. Therefore, the temperature difference at solid-fluid interface has been thought over.

Figure 2(b) depicts the left view of the part of micro-pillar arrays. The p/d is 1.0 and h/d equates to 0.5, respectively. One sets $d = 8$ and the height solid heater $H_b^* = H_b/d$ is 1.5

Figure 2(c) displays the heater (Ja = 0.15) with $Lx \times Lz = 91 \times 91$. Symmetry boundary conditions are imposed at the all sides of computation domain.

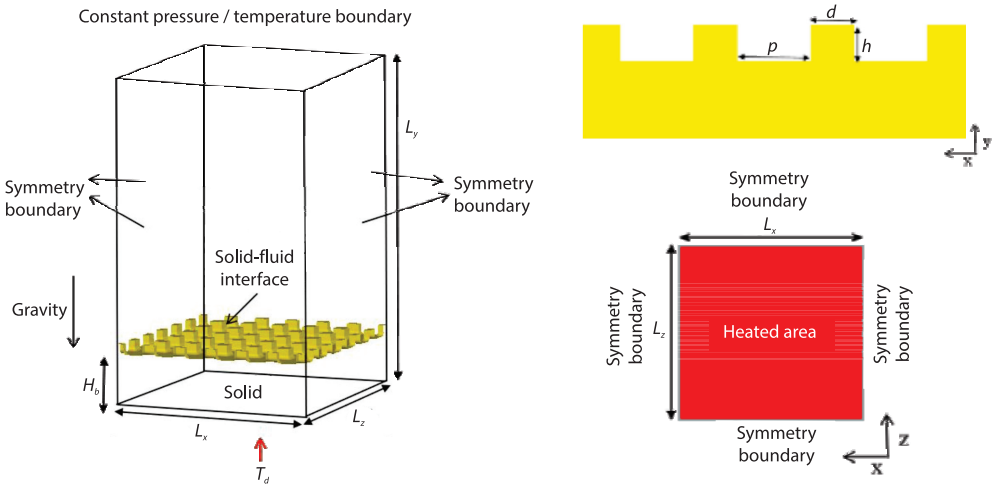

Figure 2. Schematic of computations domains; (a) computation domain, (b) part side view of S_1, and (c) bottom view of structured surface

Dimensionless parameters

The dimensionless time was defined as $t^* = t/t_0$, where

$$t_0 = \sqrt{\frac{l_0}{l_0 g_{\text{grav}}}} \quad \text{and} \quad l_0 = \sqrt{\frac{\sigma}{(\rho_\ell - \rho_\text{v})g_{\text{grav}}}}$$

The Jakob number, Ja, was defined:

$$\text{Ja} = \frac{c_{p,\ell}(T_\text{w} - T_\text{sat})}{h_{\ell\text{v}}} \tag{21}$$

The dimensionless space- and time- average boiling heat flux q' is defined:

$$q' = \frac{q_{y=H_b^*}}{q_0} = \frac{1}{S_{\text{heater}}\Delta t}\int_{t_1}^{t_1+\Delta t}\left[\int_0^{S_{\text{heater}}} k_\text{s}\left(\frac{\partial T}{\partial y}\right)_{y=0}\frac{\Delta y}{T_{\text{cr}}}\text{d}x\text{d}z\right]\frac{\text{d}t}{q_0} \tag{22}$$

where S_{heater} is the surface area of heater. The reference boiling heat flux was given:

$$q_0 = \frac{\mu_\ell h_{\ell\text{v}}}{l_0} \tag{23}$$

The stable film boiling heat flux can be expressed in dimensionless form:

$$q_{\text{film boiling}} = 0.425\left(\frac{\text{Ja}^3\text{Ar}}{\text{Pr}_\ell^2\text{Pr}_\text{v}}\right)^{1/4}\left(\frac{h'_{\ell\text{v}}}{h_{\ell\text{v}}}\right)^{1/4}\left(\frac{k_\ell}{k_\text{v}}\right)^{1/2}\left(\frac{c_{p,\text{v}}}{c_{p,\ell}}\right)^{1/2} \tag{24}$$

where

$$h'_{\text{fg}} = h_{\text{fg}} + 0.5c_{p,\text{v}}(T_\text{w} - T_\text{sat})$$

is the specific latent heat including sensible heating of vapor film. The $\text{Ar} = \rho_\text{v}\sigma l_0/\mu_\ell^2$ is the Archimedes number.

The dimensionless time-average temperature T'_w is defined:

$$T'_w = \frac{T_{y=H_b^*}}{T_w} \tag{25}$$

Result and discussions

In practice, micro-structure and wettability both play an essential role in boiling phenomena, and each one relates to the other. In order to accurately illustrate the underlying characteristic behind boiling, it is essential to know micro-structure and wetting influences by simulations.

Geometry of micro-pillar

Figures 3(a)-3(d) depicts in detail that 3-D views of the part profile for four kinds of structured surface with micro-pillar, and smooth surface is named as S_0. The same domain ($Lx \times Ly \times Lz = 91 \times 220 \times 91$) for all simulations is depicted in fig. 2.

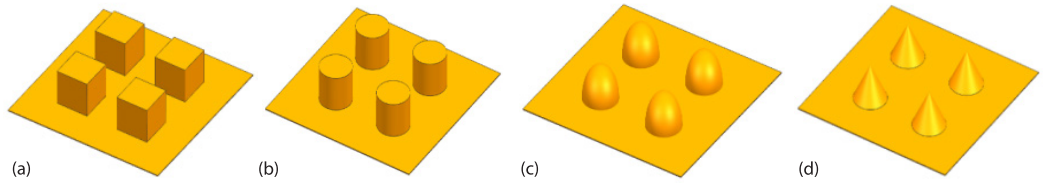

Figure 3. Part view of S_1~S_4 modified micro-pillar surface; (a) S_1 (cubic), (b) S_2 (cylindrical), (c) S_3 (spherical), and (d) S_4 (conical)

Figure 4 shows 3-D views of bubble dynamic of S_0~S_1 ($\theta = 50^o$) at Ja = 0.15. Figure 4(a) depicts that bubble first nucleated around the section where micro-pillar crossed smooth surface. The nucleate site density of S_0 was much larger than S_1 because of micro-pillar. The bubbles are denoted in light purple and solid in dark yellow. Besides, fig. 4(b) displays that bub-

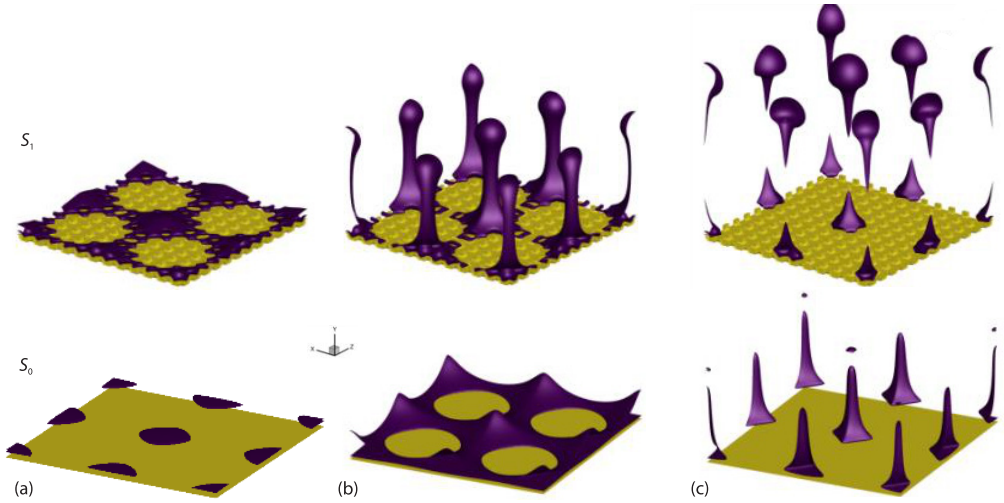

Figure 4. Vapor distribution on hydrophilic surface S_0~S_4 (at $y = H_b^*$); (a) $t^* = 84.8$, (b) $t^* = 118.8$, and (c) $t^* = 135.8$

ble merged each other [20], and local micro-pillar had been enclosed by large bubble. Region covered by large bubble on S_1 was less than S_0 due to flow resistance generated by vertical side wall. Then, as shown in fig. 4(c), once buoyancy force acting on bubble exceeded surface tension force, the bubble was going to lift off the surface. Before the first bubble detached totally from surface, its vapor-liquid interface still touched with another bubble below itself, then the second bubble was elongated slowly as the first bubble departs. It was obvious that departure diameter and time of S_0~S_1 were distinct.

In order to describe the heat transfer performance of S_0~S_4, fig. 5. displays temporal changes of the space-averaged heat flux q' through the solid-liquid surface and T_w' of surface adjacent with the fluid at Ja = 0.15 from time $t^* = 35$ to $t^* = 165$, respectively. The magenta empty circle stands for Point *a*, and the cyan empty circle relates to Point *b*. Generally, Point *a* was where lots of bubbles started to nucleate and Point *b* was where a large number of bubbles departed from heater surface. Besides, as known from fig. 5(a), q' of S_1-S_4 fell above S_0. The T_w' of S_1~S_4 fell down below S_0 except for S_4 due to increased bubble coalescence possibility [21]. Specifically speaking, the temperature and time of the onset of nucleate boiling on S_0 were 99.89% and $t^* = 102.2$, respectively. Unsurprisingly, S_1~S_3 had lower temperature than S_0, while S_4 had same temperature as S_0. All of nucleation boil processes on S_1~S_4 happened advanced than S_0. These results about S_1~S_3 pointed out that the increased surface area accounted for enhancing pool boiling heat transfer performance. As shown in figs. 5(a) and 6(a) the improvements have been attributed to decreasing the superheat for nucleation and to decreasing bubble coverage (the ratio of bubble volume to vacancy of micro-pillar).

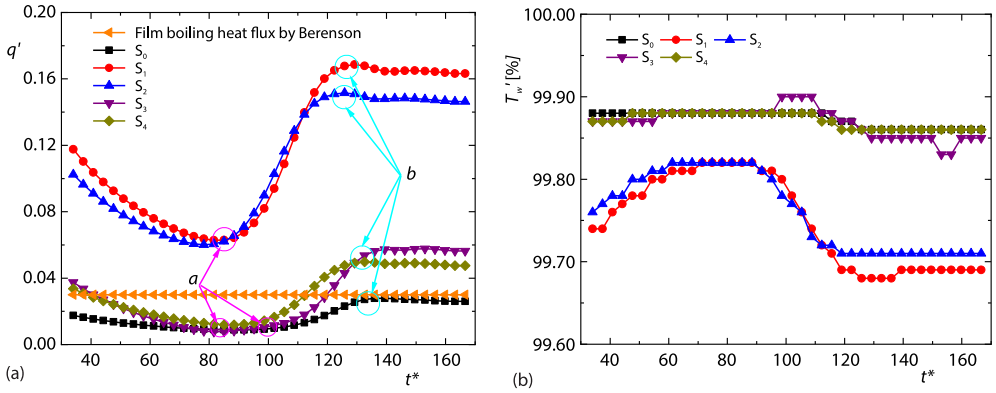

Figure 5. Geometric effects on simulated heat performance curves for infinite micro-pillar structured hydrophilic surfaces (at $y = H_b^*$); (a) transient heat flux and (b) transient wall temperature

From figs. 5(a) and 5(b), q' had the alike trend and so did T_w' curves, although S_1~S_4 indicated the various effects on boil heat transfer performance. The change of these lines could be almost divided into three parts, which were split by Points *a* and *b*.

At the first process, the T_w' curves increased slightly before bubbles nucleate, which caused the decrease of q' curves. It implied that with mainstream liquid temperature increasing up, the temperature difference between solid and liquid got small. The q' through the liquid then went down, showing a decrease generally in fig. 5(a). Among all micro-pillar surfaces, q' of S_3 ($q' = 0.009$) was lower than S_1, S_2, and S_4 while T_w' of S_4 ($T_w' = 99.97\%$) was higher than S_1-S_3, as shown in fig. 5(b) in addition, q' was the highest and T_w' of S_1 was the lowest. The results showed that the larger added area the surface of solid heater had, the better heat transfer performance at this stage was.

At the second process, T_w' curves reached their maximum at Point *a* and then began to decline. As shown in fig. 5(a), Point *a* was where bubbles started to nucleate. Namely, bubbles nucleated over S_1 at $t^* = 88.4$, over S_2 at $t^* = 86.2$, over S_3 at $t^* = 84.3$, over S_4 at $t^* = 85.1$, and over S_0 at $t^* = 102.7$. It was worth noting that bubbles firstly nucleated over S_3 and lastly nucleated over S_0. After bubbles nucleation, q' curves rise remarkably for a long time before bubbles departure while T_w' curves in fig. 5(b) decreased slightly. The transition about q' and T_w' curves indicated that due to the onset of nucleation boiling, the liquid contacting with solid wall (at $y = H_b^*$) tended to absorb lots of heat from heated surface to meet the latent heat of vaporization. For one thing, q' increased up to 0.167 for S_1, 0.150 for S_2, 0.057 for S_3, 0.049 for S_4, and 0.027 for S_0, as shown in fig. 5(a). The result illustrated that when the height and diameter were fixed, the effect of the geometry of pillar on the nucleation boiling was essential. Besides, decreasing porosity of the pillar array reinforced the capillary force what drove the liquid toward the dry spot [22], and the dry spot could be rewetted more quickly. For another thing, as shown in fig. 5(b), T_w' reduced by mostly less than 0.1%. For instance, T_w' of S_1 decreased by 0.13%, which was because of high thermal conductivity of solid.

At the third process, fig. 5(a) demonstrates that Point *b* was where bubbles departure from heater surface. In other word, the various coalesced bubbles departed from S_1 at $t^* = 129.2$, from S_2 at $t^* = 122.3$, from S_3 at time $t^* = 132.6$, from S_4 at $t^* = 125.2$, and from S_0 at $t^* = 135.8$. It should be known that bubbles firstly departed from S_2, lastly departed from S_0. One should expect the result for the q' curves of these surfaces. The q' and T_w' curves then kept nearly stable before the next nucleation boiling occurred. In addition, the bubble departure procedure of S_1~S_4 was interesting. If bubbles departed from a smooth surface, the heat transfer would drop down gradually until the next bubble nucleation. This process was named waiting period in bubble cycle. During waiting time, the surface might be reheated when departing bubbles carried thermal boundary-layer and energy from the solid surface to the bulk flow zone. However, according data from fig. 4, unlike S_0, the bubble departing from S_1~S_4 included base area shrinking and necking phenomenon. The large bubble was divided two sections: remained section and departing one, also named the first bubble and the second bubble, respectively. The remained part produced many bubbles generation seeds at once. Because of those extra bubble generation seeds, lot of newly nucleated bubbles stacked over the micro-pillar array when the heat flux was large enough, which prevented the newly grew bubbles from departing. As a result, the q' curves were going to fall down, but q' curves of S_1~S_4 were all much larger than S_0 due to bubble nucleation density.

Finally, from the data of fig. 5(b), based on heat transfer performance or bubble dynamics, micro-pillar structured surfaces were better than bare surface, which was in accord with experiments. Comparing heat transfer performance within micro-pillar structure surfaces, S_4 had the worst heat transfer performance and S_1 had the best heat transfer performance. Porosity of S_1 and S_2 was both small, which meant that expanding the area of surfaces and decreasing the porosity usually leaded to a better heat transfer performance in this simulation.

Table 1 shows characteristics of heat transfer performance and bubble dynamic of S_0~S_1. From tab. 1, one knows that q' of S_1 is higher with lowest temperature and smaller bubble coverage than S_0.

Table 1. Heat transfer process characteristics of micro-pillar and smooth surfaces

Number	q'	T'_w [%]	Bubble nucleate		Bubble coverage	Bubble departure t^*
			t^*	Count		
S_0	0.017	99.97	102.7	443	34.4%	135.8
S_1	0.117	99.84	88.4	938	14.1%	129.2
S_0 ($\theta = 130°$)	0.012	99.97	40.1	2352	100%	142.3
S_1 ($\theta = 130°$)	0.232	99.70	35.4	3254	100%	146.2
CW_2	0.621	N/A	25.1	473	11.1%	83.9
CW_5	0.401	N/A	28.4	2180	10.8%	75.5

Pure wettability

This work examines hydrophobic surface with micro-pillar to assess the effect of wettability on bubble dynamics. By changing fluid-solid effect parameters, either hydrophilic characteristic ($\theta = 50°$) or a hydrophobic characteristic ($\theta = 130°$) can be got. One should notice that the number of vapor phase means the amount of lattice node that density is vapor.

Figure 6 depicts in detail the effect of wettability of micro-pillar surface on bubble dynamics. There were three important things needed to know from fig. 6. Firstly, there were much more nucleation sites on surface ($\theta = 130°$) than on surface ($\theta = 50°$) [12]. It was the nucleation sites that resulted in the huge enhancement of heat transfer for S_1~S_4. For one thing, S_0 did not benefit from extra nucleation sites due to its low flow resistance. For another thing, vertical side wall of S_1 provided high flow resistance, which suppressed adjacent bubbles coalescence. Secondly, after bubbles departed from heated surface, there were many bubble seeds left, which would be activated soon and promote heat transfer. Lastly, hydrophobic played a more essential role in nucleate site density than cubic shaped geometry of micro-pillar did. The difference in nucleate site of S_1~S_4 ($\theta = 130°$) was not so obvious as contact corner equates to 50°.

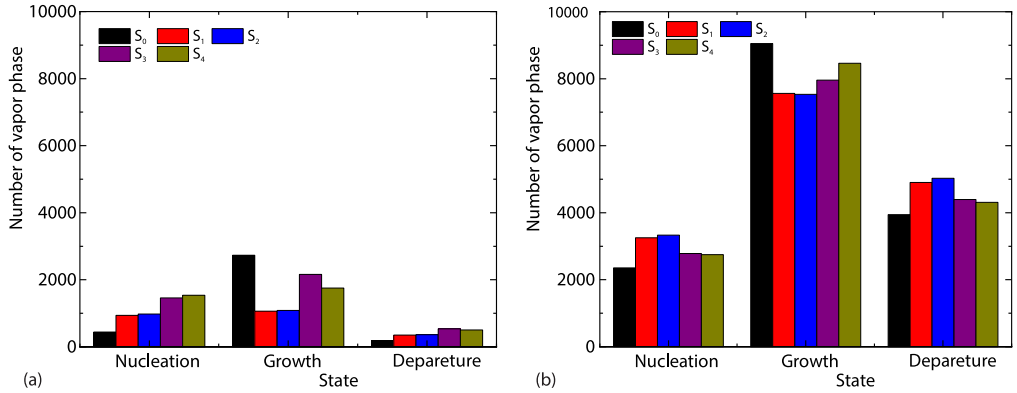

Figure 6. Amounts of vapor lattice node on different structured surfaces at Ja = 0.15; (a) micro-pillar ($\theta = 50°$) and (b) micro-pillar ($\theta = 130°$)

The q' and T'_w changes of S_1~S_4 on hydrophobic condition are depicted in figs. 7(a) and 7(b), respectively. Figure 7(a) shows that the time-averaged q' values of S_0~S_4 are 0.012, 0.232, 0.188, 0.156, and 0.094, respectively. Varying wettability increases nucleate boiling heat transfer performance for micro-pillar structured surface. This was because hydrophobic surface induced much more bubbles generation than a hydrophilic surface, as shown in fig. 7. What

is more, fig. 7(b) shows that on the condition of hydrophobic, T'_w of S_1~S_4 moved downward. These consequences showed hydrophobic surface (θ = 130°) provided more advantages for bubbles nucleation and growth than hydrophilic surface (θ = 50°). The inconsistency in boiling heat transfer between surface (θ = 130°) and surface (θ = 50°) was according to the finding.

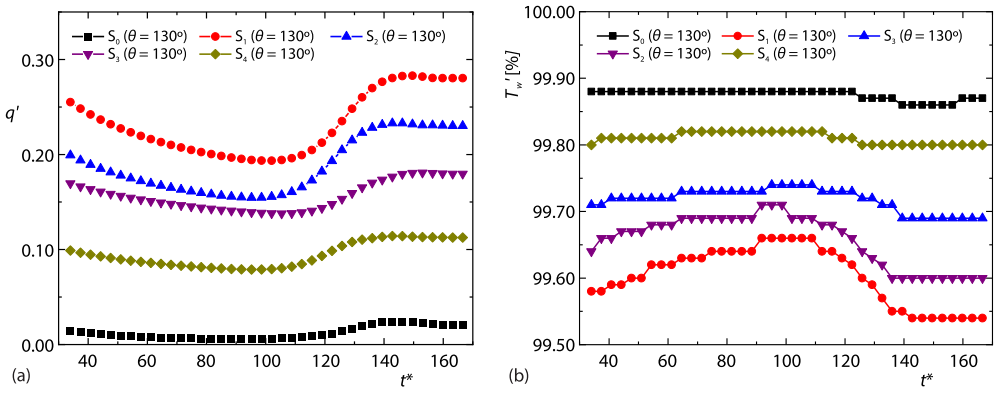

Figure 7. Wettablity influence on heat transfer curves for S_0~S_4 (at $y = H^*_b$); (a) transient heat flux and (b) transient wall temperature

As for S_0 under hydrophobic circumstance, the S_0 tended to form vapor blanket and blocks fresh liquid from flowing toward dryspot area because the vapor over smooth substrate was easy to flow around and coalesce. Thus, q' of S_0 dropped, as shown in fig. 7(a).

Table 1 shows characteristics of heat transfer performance and bubble dynamic of hydrophobic S_0~S_1. From tab. 1, one knew firstly that q' of S_1 enhanced largely compared to corresponding hydrophilic modified surface. Secondly, the effect of hydrophobic on nucleate density was much more essential than geometry of micro-pillar. The larger hydrophobic region was, the more nucleate the surface produced. Thirdly, the time of bubble departures was delayed for S_0~S_1.

Mixed wettability

Compared within S_0~S_4, whether on hydrophilic or on hydrophobic condition, the heat transfer performance of S_1 is highest with lowest wall temperature. This section studied mixed the effect of wettability on boiling heat transfer based on S_1. All kinds of surfaces with mixed wettability are showed in fig. 8. The red part in fig. 8 stands for the hydrophobic wettability area to the surface micro-pillar while the yellow part means hydrophilic.

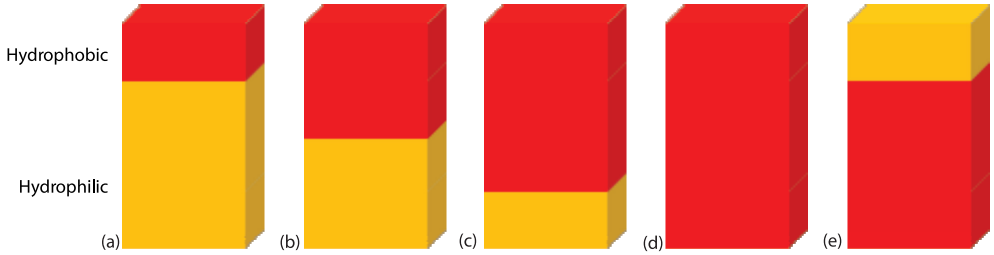

Figure 8. Hybrid wettability area of S_1; (a) CW_1, (b) CW_2, (c) CW_3, (d) CW_4, and (e) CW_5

Figure 9 depicts that q' of CW_1~CW_4 varied with time at Ja = 0.15. It was worth noticing that the boiling onset on CW_1~CW_4 happened much early, and q' enhanced greatly [23] from

fig. 9. For instance, time-average q' of CW_1 was 0.407, CW_2 was 0.621, CW_3 was 0.565, and CW_4 was 0.547, respectively, which was actually over peak of S_1, 0.167, because mixed wettability addressed formation of local vapor blanket and backflow of mainstream liquid.

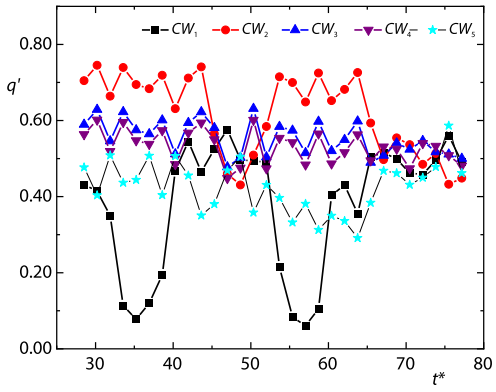

Figure 9. Heat flux of CW_1~CW_5 ($y = H_b^*$)

Specifically speaking, the nucleation site onp hydrophobic region of micro-pillar were much easier activated than on rest region of CW_1~CW_4. Due to this inhibition effects, there was no bubble formation on horizontal surface of CW_2, as shown in fig. 10i(a). Thus, flow resistance generated by vapor phase for liquid-flow decreased remarkably. Mainstream liquid then wetted heated surface under condition of capillary force and hydrophilic characteristic, and provided top of micro-pillar with liquid. Besides, fig. 10i(b) shows that the heat flux over the intersection of hydrophilic region and hydrophobic region was high while the pure wettability surfaces were low, which was consistent with bubble formation in fig. 10i(a). This was because hydrophobic surface firstly helped nucleate activate. Then, bubble covered the top hydrophobic region of micro-pillar structure, which resulted in the low heat flux of top region of micro-pillar. Otherwise, at the intersection region of wettability, bubble nucleation absorbed lots of energy to meet the need of latent heat of vaporization and growth. As a result, heat from heated surface tended to be transferred to intersection of wettability surface not to pure wettability.

Compared within CW_1~CW_4, the bad performance of CW_1 resulted from small hydrophobic region onp of micro-pillar while CW_3~CW_4 resulted from large hydrophobic region. Small hydrophobic region produced less nucleation sites and forced bubble to grow at limited region. Large hydrophobic region produced more nucleation sites. Once the diameter of bubbles is over the sum of p and d, they would actually coalescent each other. The local vapor film thus

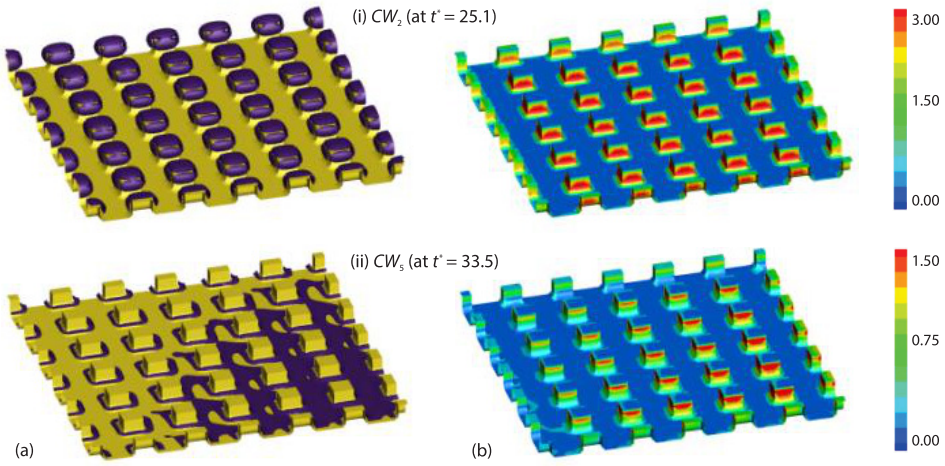

Figure 10. Density and heat flux distribution over CW_2 and CW_5

appeared. However, each part of mixed wettability region over CW_2 co-operated well, which resulted in the number of nucleation was enough and mainstream could wet heated surface.

Compared to S_1 (θ = 130º), the boiling onset on CW_5 happened much early, and q' enhanced greatly. That was, time-average q' of CW_5 was 0.402, which was actually over peak of S_1, 0.232. As for S_1 (θ = 130º), large nucleate density resulted in increasing number of small bubbles, enlarging the merge possibility for bubbles, and adding the heated surface area covered by vapor blanket. However, top hydrophilic region over top of micro-pillar in CW_5 restricted bubbles to cover top region of micro-pillar, stopped local vapor blanket formatting, as shown in fig. 10ii(a). Meanwhile, fig. 10ii(b) shows that q' of side wall micro-pillar was much larger than top. However, q' of CW_5 was less than CW_2 by comparing fig. 10(b).

Table 1 shows summarize of heat transfer performance and bubble dynamic of mixed wettability CW_2 and CW_5. From tab. 1, one was aware of that q' of CW_2 and CW_5 improved largely compared to corresponding pure wettability surface. Secondly, their nucleate number increased and bubble nucleation happened early. Thirdly, the bubble coverage of CW_2 decreased when CW_5 decreased remarkably.

Finally, compared with S_0, q' of S_1 was enhanced because of suppressing bubble merge. Compared with S_1, S_1 (θ = 130º) helped nucleate activate. The CW_2 controlled nucleation location, restricted bubble growth, and improved liquid backflow. The CW_5 controlled nucleate position, restricted vapor blanket formation.

Conclusions

In this paper, simulations of pool boiling heat transfer were conducted based on the 3-D pseudo-potential LBM. Geometries of micro-pillar, pure wettability conditions, and special hybrid wettability conditions were investigated in order. The conclusions are as follows.

- Because micro pillar served as artificial nucleation sites, boiling incipience of surface with micro pillar, S_1~S_4, toke place ahead than smooth surface S_0, and bubbles preferably nucleated at bottom of micro pillar. Specifically speaking, curved side wall prompted bubble nucleation while vertical side wall restricted bubble coalescence. So heat flux q' of cubic micro pillar surface S_1 was 0.117 while conical micro pillar S_4 was 0.030.
- Cubic micro pillar surface S_1 with hydrophobic wettability indicated greater heat transfer performance due to extra nucleation sites, lower nucleation temperature than hydrophilic surface. Thus, q' of S_1 with hydrophobic wettability added by 98.3%.
- Heat flux of cubic micro pillar surfaces with hybrid wettability, CW_1~CW_5, improved remarkably than cubic micro pillar surface S_1 with pure wettability, and so did flow field in phase change region. For instance, q' of CW_2 increased by 430.7%.

This work only pays its attention on pool boiling of regular micro-structure surfaces. It is worthwhile to simulate pool boiling of random porous micro-structure surfaces. Besides, superhydrophilic and superhydrophobic surfaces also should be investigated.

Nomenclature

c_s – lattice sound speed, [ms^{-1}]
c_0 – pesudopotential coefficient
c_p, c_v – specific heat capacity, [Jkg^{-1}K^{-1}]
e_i – lattice velocity, [ms^{-1}]
F – force, [N]
f_i – density distribution, [kgm^{-3}]
g – gravity accelerator, [ms^{-2}]
g_i – temperature distribution, [K]
h – latent heat of vaporization, [KJkg^{-1}]
Ja – Jakob number
p – pressure, [Pa]
q – heat flux, [Jm^{-2}s^{-1}]
R – universe gas constant, [Jkg^{-1}K^{-1}]
T – temperature, [K]

t – time, [second]
u – velocity, [ms^{-1}]
V – volumek, [m^3]
w – eccentric factor
x – position, [m]

Greek symbols

λ – thermal conductivity, [Wm^{-1}K^{-1}]
ν – dynamic viscosity, [m^{2}s^{-1}]
ρ – density, [kgm^{-3}]
τ – relaxation time
Φ – heat source, [Wm^{-3}]
ψ – density pesudopotential
ω – weighting factor

Subscripts and superscripts

ads – fluid-solid influence
aver – average
coh – fluid-fluid influence
cr – critical
eq – equilibrium
f – fluid
g – gravity
i – velocity direction
ℓ – liquid
s – solid
w – wall
v – vapor

Acknowledgment

This research work was sponsored by National Natural Science Foundation of China (Grant No. 52006218).

References

[1] Ren, T., *et al*., A Review of Small Heat Pipes for Electronics, *Applied Thermal Engineering Design Processes Equipment Economics*, *96* (2016), Mar., pp. 1-17
[2] Cong, B., *et al*., Investigation on the Heat Dissipation of High Heat Flux Chip Array by Fractal Micro-Channel Networks, *Thermal Science*, *27* (2023), 1B, pp. 869-880
[3] Lei, X., *et al.*, Study on Flow and Heat Transfer Characteristics of Cooling Channel Filled with X-Shaped Truss Array, *Thermal Science*, *27* (2023), 1B, pp. 739-754
[4] Haq, K., *et al.*, Analysis of Periodic Heat Transfer through Extended Surfaces, *Thermal Science*, *27* (2023), 3B, pp. 2549-2564
[5] Ye, M. Z., *et al*., Effects of Elastic Pillars on Fluid-Flow and Heat Transfer Enhancement in a Micro-Channel, *Thermal Science*, *27* (2023), 1A, pp. 275-287
[6] Xin, K., *et al.*, Experimental Study of Pool Boiling Heat Transfer on Novel Bistructured Surfaces Based on Micro-Pin-Finned Structure, *Experimental Thermal and Fluid Science*, *9* (2018), Feb., pp. 9-19
[7] Shen, B., *et al.*, Enhanced Pool Boiling of Ethanol on Wettability-Patterned Surfaces, *Applied Thermal Engineering*, *149* (2018), Feb., pp. 325-331
[8] Koukoravas, T. P., *et al.*, Experimental Investigation of a Vapor Chamber Featuring Wettability-Patterned Surfaces, *Applied Thermal Engineering*, *178* (2020), 115522
[9] Jo, H., *et al*., Single Bubble Dynamics on Hydrophobic-Hydrophilic Mixed Surfaces, *International Journal of Heat and Mass Transfer*, *93* (2016), Feb., pp. 554-565
[10] Kousalya, A. S., *et al.*, Heterogeneous Wetting Surfaces with Graphitic Petal-Decorated Carbon Nanotubes for Enhanced Flow Boiling, *International Journal of Heat and Mass Transfer*, *87* (2015), Aug., pp. 380-389
[11] Xie, X., *et al*., Thermal Performance of the Flat Micro-Heat Pipe with the Wettability Gradient Surface by Laser Fabrication, *International Journal of Heat and Mass Transfer*, *125* (2018), Oct., pp. 658-669
[12] Bourdon, B., *et al.*, Wettability Influence on the Onset Temperature of Pool Boiling: Experimental Evidence on Ultra-Smooth Surfaces, *Advances in Colloid and Interface Science*, *221* (2015), July, pp. 34-40
[13] Hu. Y., *et al.*, Thermal Performance Enhancement of Grooved Heat Pipes with Inner Surface Treatment, *International Journal of Heat and Mass Transfer*, *67* (2013), Dec., pp. 416-419
[14] Huang, Q., *et al.*, Numerical Study on the Effect of Thermal Diffusivity Ratio in Phase Change Heat Transfer of Crude-Oil Using Lattice Boltzmann method, *Thermal Science*, *27* (2023), 2B, pp. 1627-1639
[15] Zhou, P., *et al*., Lattice Boltzmann Simulation of Nucleate Boiling in Micro-Pillar Structured Surface, *International Journal of Heat and Mass Transfer*, *131* (2019), Mar., pp. 1-10
[16] Li, W. X., *et al*., Nucleate Boiling Enhancement by Structured Surfaces with Distributed Wettability-Modified Regions: A Lattice Boltzmann Study, *Applied Thermal Engineering*, *194* (2021), 117130
[17] Mu, Y. T., *et al.,* Nucleate Boiling Performance Evaluation of Cavities at Mesoscale Level, *International Journal of Heat and Mass Transfer*, *106* (2017), Mar., pp. 708-719

[18] Jiang, M. X., *et al*., Optimization of Micro-Channel Heat Sink with Trapezoidal Cavities and Solid/Slotted Oval Pins Based on Genetic Algorithm and Back Propagation Neural Network, *Thermal Science*, *27* (2023), 1A, pp. 179-193
[19] He, X., *et al.*, Analytic Solutions of Simple Flows and Analysis of Non-Slip Boundary Conditions for the Lattice Boltzmann BGK Model, *Journal of Statistical Physics*, *87* (1997), Apr., pp. 115-136
[20] Zhang, Y, *et al*., Nucleate Pool Boiling Heat Transfer on a Micro-Pin-Finned Surface in Short-Term Microgravity, *Heat Transfer Engineering*, *38* (2016), 6, pp. 594-610
[21] A C H, ., Nucleation Site Interaction Between Artificial Cavities during Nucleate Pool Boiling on Silicon with Integrated Micro-Heater and Temperature Micro-Sensors, *International Journal of Heat and Mass Transfer*, *55* (2012), 11-12, pp. 2769-2778
[22] Cao, Z., *et al*., Pool boiling Heat Transfer of FC-72 on Pin-Fin Silicon Surfaces with Nanoparticle Deposition, *International Journal of Heat and Mass Transfer*, *126* (2018), Part A, pp. 1019-1033
[23] Betz, *et al*., Boiling Heat Transfer on Superhydrophilic, Superhydrophobic, and Superbiphilic Surfaces, *International Journal of Heat and Mass Transfer*, *57* (2013), 2, pp. 733-741

Paper submitted: January 14, 2023
Paper revised: April 17, 2023
Paper accepted: April 17, 2023